

# Integrated Optical Coherence Tomography and Microscopy for *Ex Vivo* Multiscale Evaluation of Human Breast Tissues

Chao Zhou<sup>1</sup>, David W. Cohen<sup>2</sup>, Yihong Wang<sup>2,3</sup>, Hsiang-Chieh Lee<sup>1</sup>, Amy E. Mondelblatt<sup>2</sup>, Tsung-Han Tsai<sup>1</sup>, Aaron D. Aguirre<sup>1,4</sup>, James G. Fujimoto<sup>1</sup>, and James L. Connolly<sup>2</sup>

## Abstract

Three-dimensional (3D) tissue imaging methods are expected to improve surgical management of cancer. In this study, we examined the feasibility of two 3D imaging technologies, optical coherence tomography (OCT) and optical coherence microscopy (OCM), to view human breast specimens based on intrinsic optical contrast. Specifically, we imaged 44 *ex vivo* breast specimens including 34 benign and 10 malignant lesions with an integrated OCT and OCM system developed in our laboratory. The system enabled 4- $\mu$ m axial resolution (OCT and OCM) with 14- $\mu$ m (OCT) and 2- $\mu$ m (OCM) transverse resolutions, respectively. OCT and OCM images were compared with corresponding histologic sections to identify characteristic features from benign and malignant breast lesions at multiple resolution scales. OCT and OCM provide complimentary information about tissue microstructure, thus showing distinctive patterns for adipose tissue, fibrous stroma, breast lobules and ducts, cysts and microcysts, as well as *in situ* and invasive carcinomas. The 3D imaging capability of OCT and OCM provided complementary information to individual 2D images, thereby allowing tracking features from different levels to identify low-contrast structures that were difficult to appreciate from single images alone. Our results lay the foundation for future *in vivo* optical evaluation of breast tissues, using OCT and OCM, which has the potential to guide core needle biopsies, assess surgical margins, and evaluate nodal involvement in breast cancer.

*Cancer Res*; 70(24): 10071–9. ©2010 AACR.

## Introduction

Excluding skin cancers, breast cancer has the highest incidence in women, with an estimated 207,090 new cases of invasive breast carcinoma and 54,010 new cases of *in situ* carcinoma expected to occur in the United States in 2010 (1). Even though breast cancer is the second leading cause of cancer death in women, with an estimated 39,840 occurring in 2010, breast cancer mortality has declined in the last decade. This decrease in mortality is largely attributed to the increased use of screening mammography and the improved effectiveness of treatments (1). Image-guided core biopsy and surgical

excisional biopsy are most often used in the diagnostic workup of breast lesions. Compared with open surgical biopsy, core biopsy is less invasive and is therefore considered a gold standard for the diagnosis of breast cancer (2). However, core biopsy has the disadvantage of false-negative rates that result from limitations in tissue sampling (3–6). The false-negative rate for palpation-guided and stereotactic guided core biopsy ranges from 0%–13% (5, 7) to 0.2%–8.9% (5, 8), respectively. Ultrasound-guided core biopsy has been shown to reduce the false-negative rate to 0%–3.6% (5, 6, 9, 10). Imaging techniques providing more accurate sampling capabilities in real-time are desirable for improving the diagnostic performance of core biopsies. The emergence of breast-conserving surgical procedures, such as partial mastectomy, allows preservation of the breast without compromising survival. The surgical margin status is considered a strong predictor for local recurrence following partial mastectomy (11–13). In clinical practice, the combination of intraoperative gross examination and post-operative histologic examination is employed to evaluate the surgical margins. However, approximately 40% of patients require a second surgical procedure due to positive or close margins (14, 15). In addition, evaluation of sentinel and axillary nodal involvement is critical for staging breast cancers (16, 17). Postoperative histologic examination remains the gold standard in assessing the status of lymph nodes. However, sentinel and axillary lymph node resections may lead to potential complications such as lymphedema (18). Frozen section analysis has been used to evaluate the status of

**Authors' Affiliations:** <sup>1</sup>Department of Electrical Engineering and Computer Science and Research Laboratory of Electronics, Massachusetts Institute of Technology, Cambridge, Massachusetts; <sup>2</sup>Department of Pathology, Beth Israel Deaconess Medical Center, Harvard Medical School, Boston, Massachusetts; <sup>3</sup>Department of Pathology, Montefiore Medical Center and Albert Einstein Medical School, Bronx, New York; and <sup>4</sup>Harvard-MIT Division of Health Sciences and Technology, Cambridge, Massachusetts

**Note:** Supplementary data for this article are available at Cancer Research Online (<http://cancerres.aacrjournals.org/>).

**Corresponding Author:** James L. Connolly, Department of Pathology, Beth Israel Deaconess Medical Center, 330 Brookline Avenue, Boston, MA 02215. Phone: 617-667-5754; Fax: 617-975-5620. E-mail: [jconnoll@bidmc.harvard.edu](mailto:jconnoll@bidmc.harvard.edu)

doi: 10.1158/0008-5472.CAN-10-2968

©2010 American Association for Cancer Research.

surgical margins and nodes intraoperatively (19, 20). However, the analysis is time-consuming and the sampling area is limited. Therefore, a real-time, nondestructive imaging method that has a large sampling field, micron-scale resolution, and depth-resolved imaging capability are desirable for the intraoperative evaluation of breast cancer.

Optical coherence tomography (OCT) is a promising technique for real-time, high-resolution imaging of tissue morphology (21) and has the potential to be used for these important clinical applications. OCT images are formed by detecting back-reflected light, instead of sound, from tissues and therefore enable an order of magnitude in improved imaging resolution compared with ultrasound. Recently, OCT has been used to evaluate breast lesions in animal models (22) and in humans (23). Pilot studies have also used OCT for evaluating lymph nodes (24) and intraoperative surgical margin status (25) in breast cancer. To maintain a large imaging depth in OCT, the transverse resolution is usually limited to 10–20  $\mu\text{m}$ , which is not sufficient to image cellular features. Optical coherence microscopy (OCM) is a combination of OCT and confocal microscopy that achieves cellular imaging resolution in both the transverse and axial planes (26–28). By enhancing the filtration of multiply scattered light, better image contrast and greater imaging depth are achieved with OCM (29) with lower numerical aperture compared with confocal microscopy.

In this study, we employ an integrated OCT and OCM system developed in our laboratory to study freshly excised human breast tissue with various pathologic diagnoses *ex vivo*, based on intrinsic optical contrast. Integrated OCT and OCM has the additional advantage of enabling investigation of tissue structure at the architectural and cellular scales, in a way similar to traditional light microscopy. Few studies using integrated OCT and OCM imaging have been conducted to date (30, 31), largely due to the lack of advanced OCM instrumentation. The objective of our study is to establish certain imaging features observed in OCT and OCM and compare them with histology to identify characteristic features of breast lesions that can be visualized with OCT and OCM. The results provide a basis to interpret future OCT and OCM breast tissue images and lay the foundation for future *in vivo* optical evaluation of breast lesions.

## Materials and Methods

### Instrumentation

A portable, integrated time-domain 3D-OCT and 3D-OCM system was employed for this study. A detailed description of the system can be found in Aguirre (32). Briefly, a compact, spectrally broadened, femtosecond Nd:Glass laser was used as the light source to provide >200-nm bandwidth centered at 1,060 nm. This enables a <4- $\mu\text{m}$  axial resolution for the OCT and OCM subsystems, providing optical image slices thinner than traditional histologic sections. The transverse resolution was  $\sim 14$  and 2  $\mu\text{m}$  for the OCT and OCM subsystems, respectively. Objectives for OCT and OCM were turret mounted on the sample arm to allow seamless switching between high (OCM) and low (OCT) magnifications. The ability to visualize tissue morphology at multiple scales is

important for pathologists to differentiate clinically relevant features. Cross-sectional OCT images with  $1,344 \times 1,000$  ( $X \times Z$ ) pixels were acquired at 1 frame/s. A 3D-OCT data set was constructed with 640 cross-sectional scans covering a volume of  $1.5 \times 3 \times 1.3 \text{ mm}^3$  ( $Y \times X \times Z$ ). OCM images were obtained with rapid *en face* raster scanning over a  $400 \times 400\text{-}\mu\text{m}^2$  field ( $500 \times 750$  pixels) at 2 frames/s. 3D-OCM data sets were obtained on selected samples by translating the sample stage in the axial direction at 5  $\mu\text{m/s}$ . A detection sensitivity of  $-98$  dB was achieved with  $\sim 10$  mW of incident power on the samples.

### Study protocol and imaging procedures

The study protocol was approved by the institutional review boards at Beth Israel Deaconess Medical Center (BIDMC) and Massachusetts Institute of Technology (MIT). The protocol was given exempted status because discarded human tissue was collected without interfering with routine pathologic examination. Freshly excised breast specimens were selected based on the presence of pathologic findings from gross examination. Fresh tissue (typically measuring  $1 \times 1 \times 0.5 \text{ cm}^3$ ) from surgical specimens was collected for imaging and placed in RPMI medium 1640 (Invitrogen) within 1 hour following surgical excision. Imaging was performed within approximately 2–6 hours of tissue procurement. In total, 44 breast specimens were imaged from 22 patients (median age, 51 years; range, 20–90). Thirty-four benign breast specimens were imaged. The specimens with benign diagnosis include fibroadenoma ( $n = 4$ ), benign fibrocystic disease ( $n = 13$ ), fat necrosis ( $n = 3$ ), usual ductal hyperplasia (UDH;  $n = 4$ ), and normal breast parenchyma ( $n = 14$ ). Ten specimens, including invasive ductal carcinoma ( $n = 5$ ), invasive lobular carcinoma ( $n = 4$ ), mucinous (colloid) carcinoma ( $n = 1$ ), ductal carcinoma *in situ* (DCIS;  $n = 5$ ), and lobular carcinoma *in situ* (LCIS;  $n = 2$ ), were diagnosed as breast carcinoma. On average, 1.4 3D-OCT data sets (range, 1–5) and 1,011 *en face* OCM images (range, 449–2,566) were obtained from each specimen. Specimens were classified on the basis of histologic diagnosis by experienced pathologists.

Before imaging, a cover slip was gently placed on the specimen to create a flat surface and reduce optical aberration. The light pressure applied to the specimen is presumed not to influence tissue morphology and histologic comparison with OCT/OCM imaging. 3D-OCT and *en face* OCM images were acquired within the same sample area to ensure good coregistration. After imaging, a gross photograph was taken before the specimen was marked with black and red ink on the imaging surface to indicate specimen orientation. The specimen was then submitted in formalin for standard histologic processing. Five-micron sections were cut from formalin-fixed, paraffin-embedded tissue. Slides were stained with hematoxylin and eosin (H&E).

### Image analysis

*En face* slices of OCT images ( $3 \times 1.5 \text{ mm}^2$ ) were reconstructed from the 3D data sets by averaging over 10- $\mu\text{m}$  intervals in the axial direction to reduce speckle noise (31). *En face* visualization of OCT data has the advantage that the



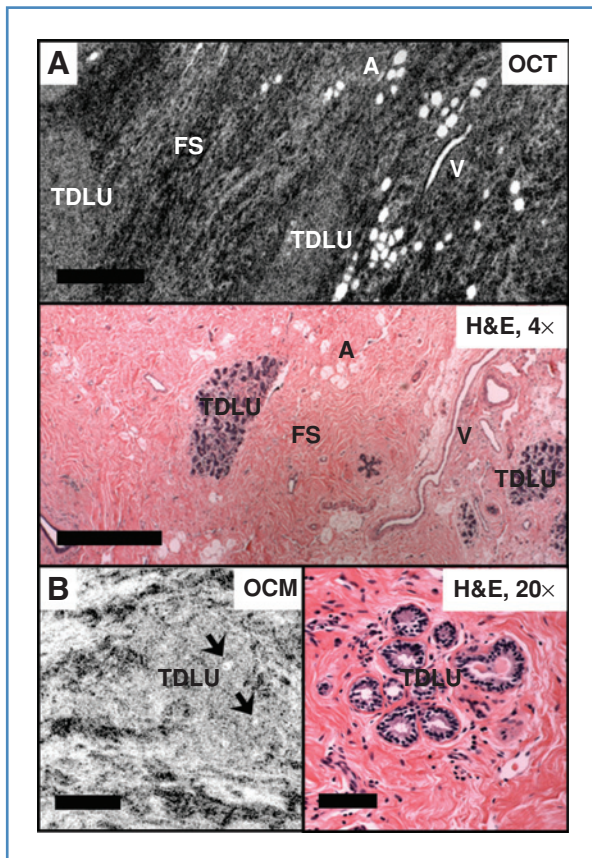


**Figure 1.** Normal breast tissues. A, *en face* OCT image ( $\sim 90\ \mu\text{m}$  beneath the tissue surface) and corresponding H&E histologic section show features such as breast TDLUs, fibrous stroma (FS), adipose tissue (A), and blood vessels (V) in normal breast tissue. Scale bars,  $500\ \mu\text{m}$ . B, OCM ( $\sim 30\ \mu\text{m}$  beneath the tissue surface) and corresponding histologic section demonstrate TDLUs at a higher magnification. Glandular lumina can be clearly seen as hyposcattering circles (arrow). Scale bars,  $100\ \mu\text{m}$ .

entire image plane is within constant focus and has similar intensity levels. The *en face* OCT and OCM images were contrast adjusted and displayed with an inverse grayscale colormap, in which black represents increased reflectivity. In this retrospective study, the entire *en face* OCT and OCM database and corresponding histology slides were reviewed to identify matching features that were seen in both OCT/OCM and histologic sections. The generation of volumetric OCT and OCM data provides more comprehensive image information than individual 2D images alone and facilitates the interpretation of OCT and OCM imaging features. Representative benign and malignant specimens were selected for presentation. Photomicrographs of matching histologic sections were taken to provide further comparison with the *en face* OCT and OCM images. Photomicrographs were digitally acquired using a standard microscope (Olympus BX40).

## Results

Figures 1 and 2 show characteristic features observed in normal breast tissue. Adipose tissue is apparent on OCT and

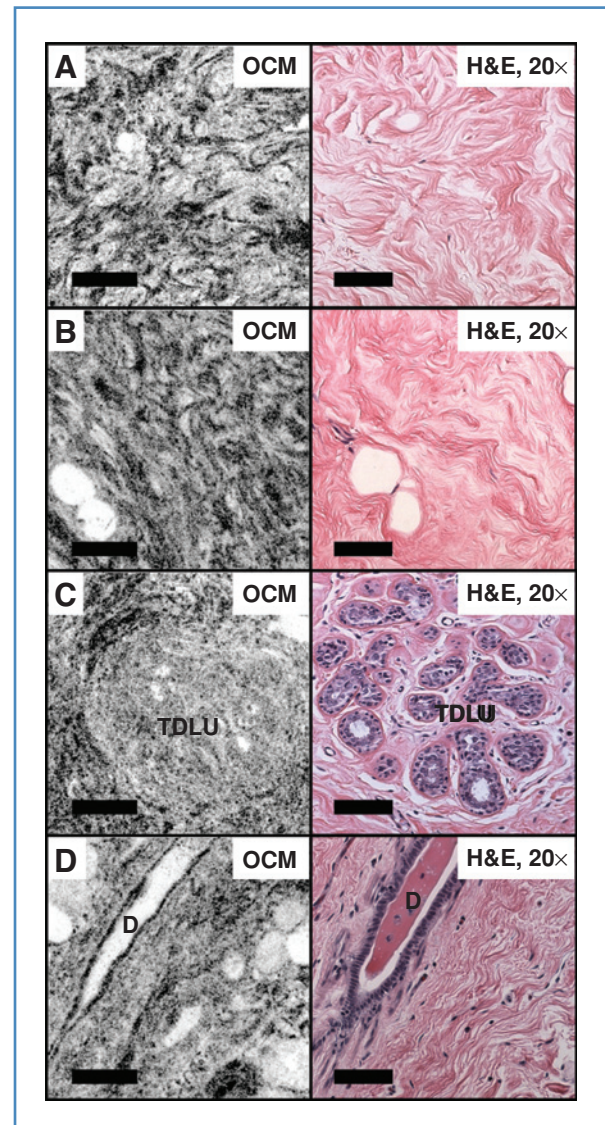


**Figure 2.** OCM images ( $\sim 50\ \mu\text{m}$  beneath the tissue surface) and corresponding H&E histologic section of normal breast tissue. Fibrous stroma (A and B); TDLUs (C); and a single interlobular duct (D). Scale bars,  $100\ \mu\text{m}$ . A 3D-OCM reconstruction of normal breast lobules can be found in the supplementary materials (Video S1).

OCM images and is visible as round hyposcattering monomorphous circular structures. Large blood vessels and/or interlobular ducts can also be easily identified as long hyposcattering tubes with hyperscattering walls. Most normal breast tissue consists of fibrous stroma, which has high collagen content and is birefringent. Therefore, loose fibrous stroma appears in the OCT/OCM images as angulated black-and-white short linear reticulation with high contrast. Compared with fibrous stroma, epithelial cell nuclei have lower backscattering. As a result, normal breast terminal duct lobular units (TDLU) appear as pale areas that are relatively homogeneous in the OCT images. Under high magnification



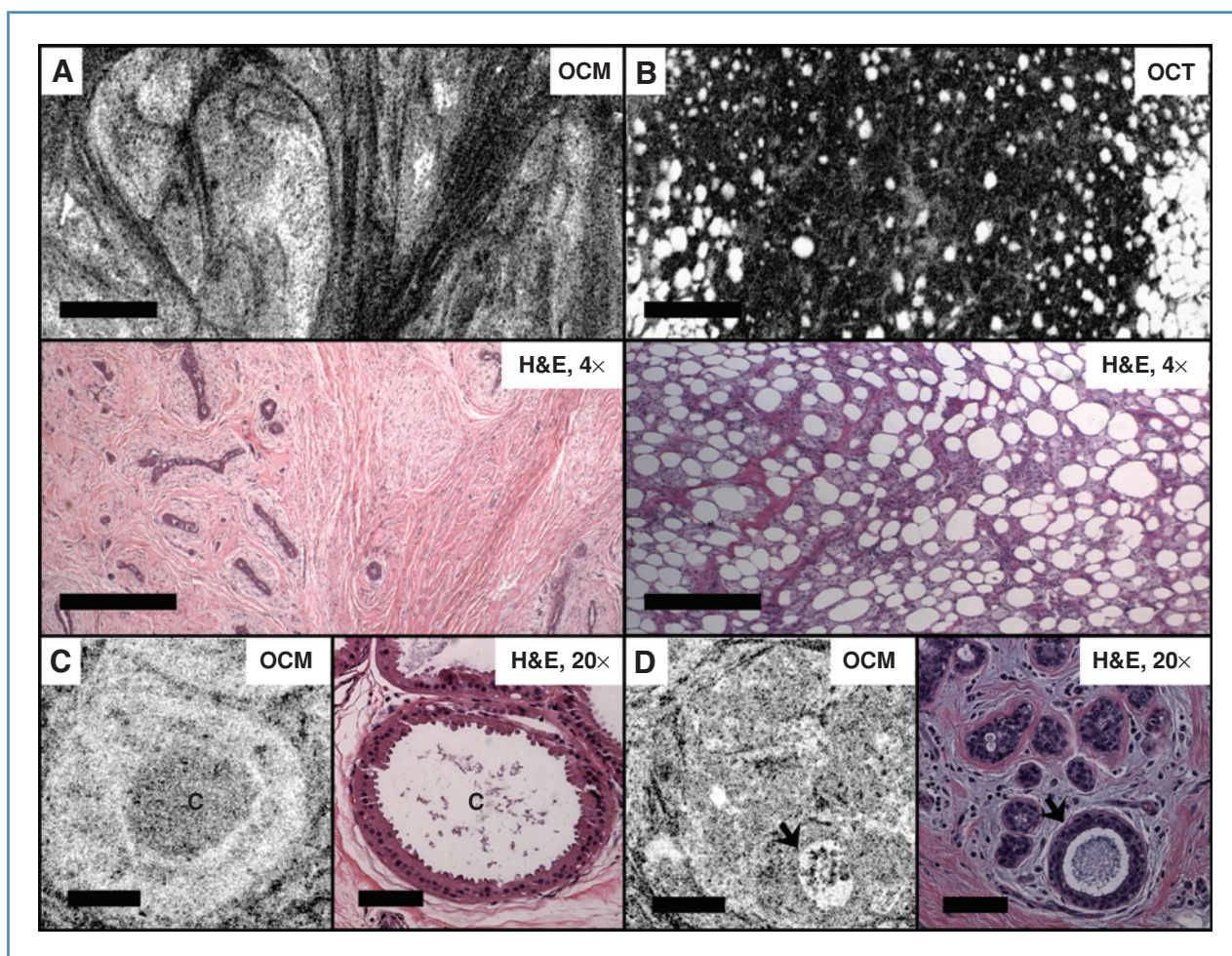


**Figure 3.** Benign breast lesions. A, OCT (120  $\mu\text{m}$  beneath the tissue surface) and corresponding H&E histologic section of a fibroadenoma; scale bars, 500  $\mu\text{m}$ . B, OCT (60  $\mu\text{m}$  beneath the tissue surface) and corresponding H&E histologic section of fat necrosis; scale bars, 500  $\mu\text{m}$ . C and D, OCM ( $\sim 150$  and  $\sim 50$   $\mu\text{m}$  beneath the tissue surface, respectively) and corresponding H&E histologic section of small cysts (C) with apocrine metaplasia and a dilated/cystic gland (arrow). Scale bars, 100  $\mu\text{m}$ . 3D-OCM reconstruction of the cyst with apocrine metaplasia can be found in the supplementary materials (Video S2).

with OCM, individual TDLU can be clearly identified with hyposcattering lumina.

Figure 3 shows several representative features observed in benign breast lesions. Figure 3A is an example of a fibroadenoma in which breast ducts are compressed by surrounding stroma. The OCT image shows the well-circumscribed nodule on low magnification; the interface consists of a smooth border separating hyperscattering dense fibrous tissue. Figure 3B shows characteristic features of fat necrosis, in which necrotic (hyposcattering) adipocytes of different sizes can be clearly identified in the OCT image. Furthermore, OCT and OCM images can also identify cysts and microcysts. Figure 3C shows an example of cysts with apocrine metaplasia in which cysts ( $\sim 400$   $\mu\text{m}$  in diameter) with a prominent epithelial lining are clearly seen. Figure 3D is another example in which a dilated gland with secretions (arrow) can be clearly identified.

Figures 4–6 show OCT and OCM images with features observed in malignant breast lesions. Figure 4A shows an

example of classic mucinous carcinoma, which is an uncommon type of invasive carcinoma that accounts for approximately 2% to 3% of all cases. The characteristic dissecting mucin with "floating" tumor cells is clearly reflected in the OCT image. Figure 4B is a case of invasive ductal carcinoma in which (pale) tumor cells infiltrating the surrounding adipose tissue are seen. Figure 4C shows a high-grade invasive ductal carcinoma. In this case, sheets of (pale) invading cells with irregular borders infiltrate the surrounding hyperscattering (dark) fibrous stroma are clearly visible. In another case of high-grade invasive ductal carcinoma (Fig. 4D), the infiltrating tumor is completely solid with a pushing border that is clearly seen with OCT imaging.

Figure 5A shows an invasive ductal carcinoma with coexisting DCIS (arrows) observed in the OCT image. The area of DCIS is clearly delineated by a basement membrane within a background of hyperscattering stromal tissue. In addition, the OCM image in Figure 5B also shows small clusters of



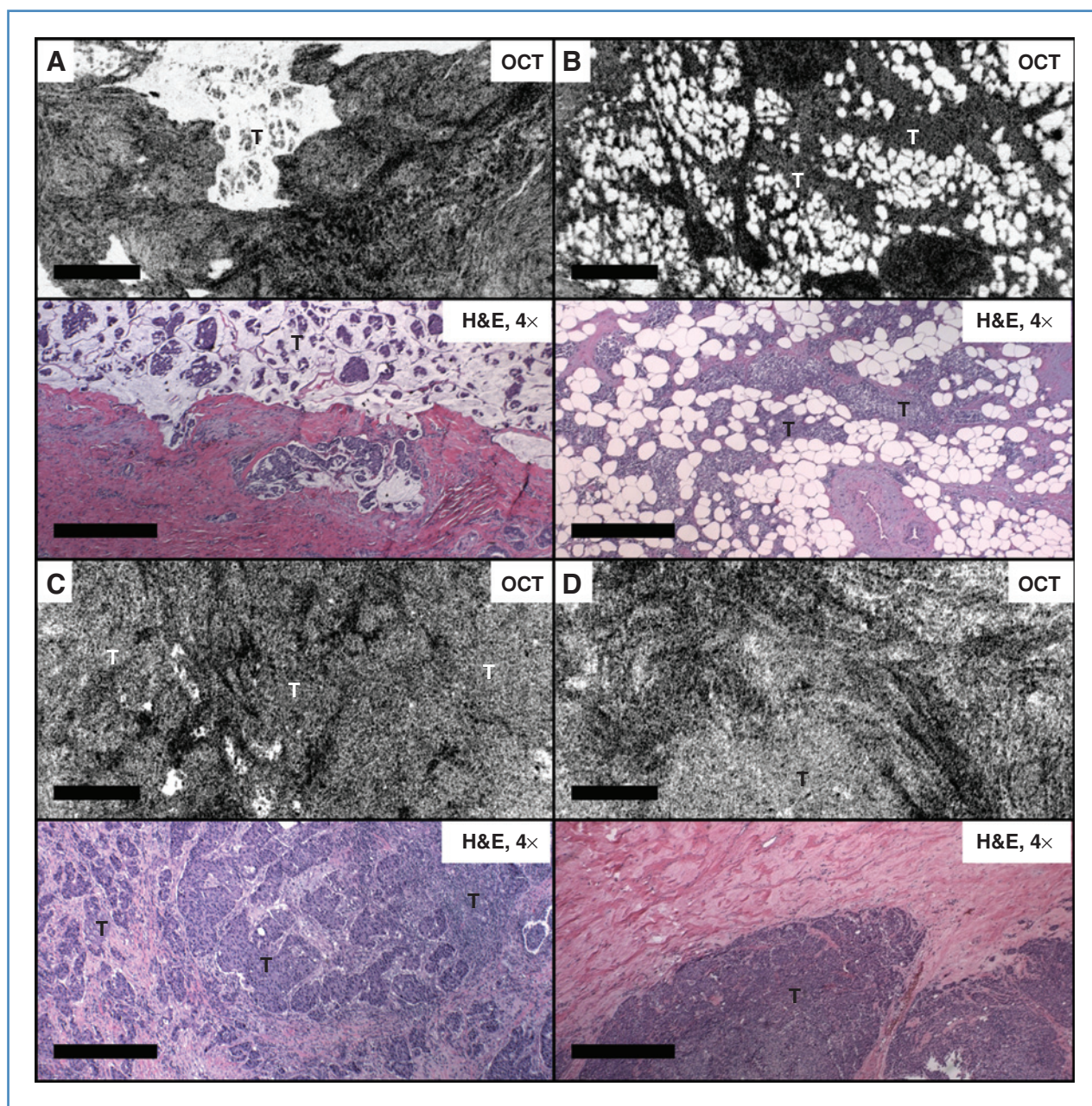


**Figure 4.** OCT images and corresponding H&E histologic sections of invasive carcinoma. A, mucinous (colloid) carcinoma (~100  $\mu\text{m}$  beneath the tissue surface). B–D, invasive ductal carcinoma (~50, ~80, and ~150  $\mu\text{m}$  beneath the tissue surface, respectively). T, tumor; scale bars, 500  $\mu\text{m}$ .

infiltrating carcinoma. In Figure 5C and D, a linear infiltration pattern characteristic of invasive lobular carcinoma can be observed with OCT and OCM imaging. Although individual invasive carcinoma cells are not directly seen in the OCT and OCM images, the stromal changes that surround the characteristic cellular infiltration show up prominently in OCT and OCM images as individual straight hyperscattering lines (arrows), mirroring the histologic features of invasive lobular carcinoma. A microvessel (V) is also observed from the OCM

image as a double line (Figure 5D) and it correlates with the vessel seen from the histologic section.

OCM images shown in Figure 6 compare features observed in *in situ* and invasive breast carcinoma. Figure 6A and B show two examples of LCIS, and Figure 6C shows an example of DCIS. As observed in the OCM images and corresponding videos provided in the supplementary materials (Videos S3 and S4), *in situ* carcinoma appears well circumscribed with a regular contour and is clearly confined within the stroma.



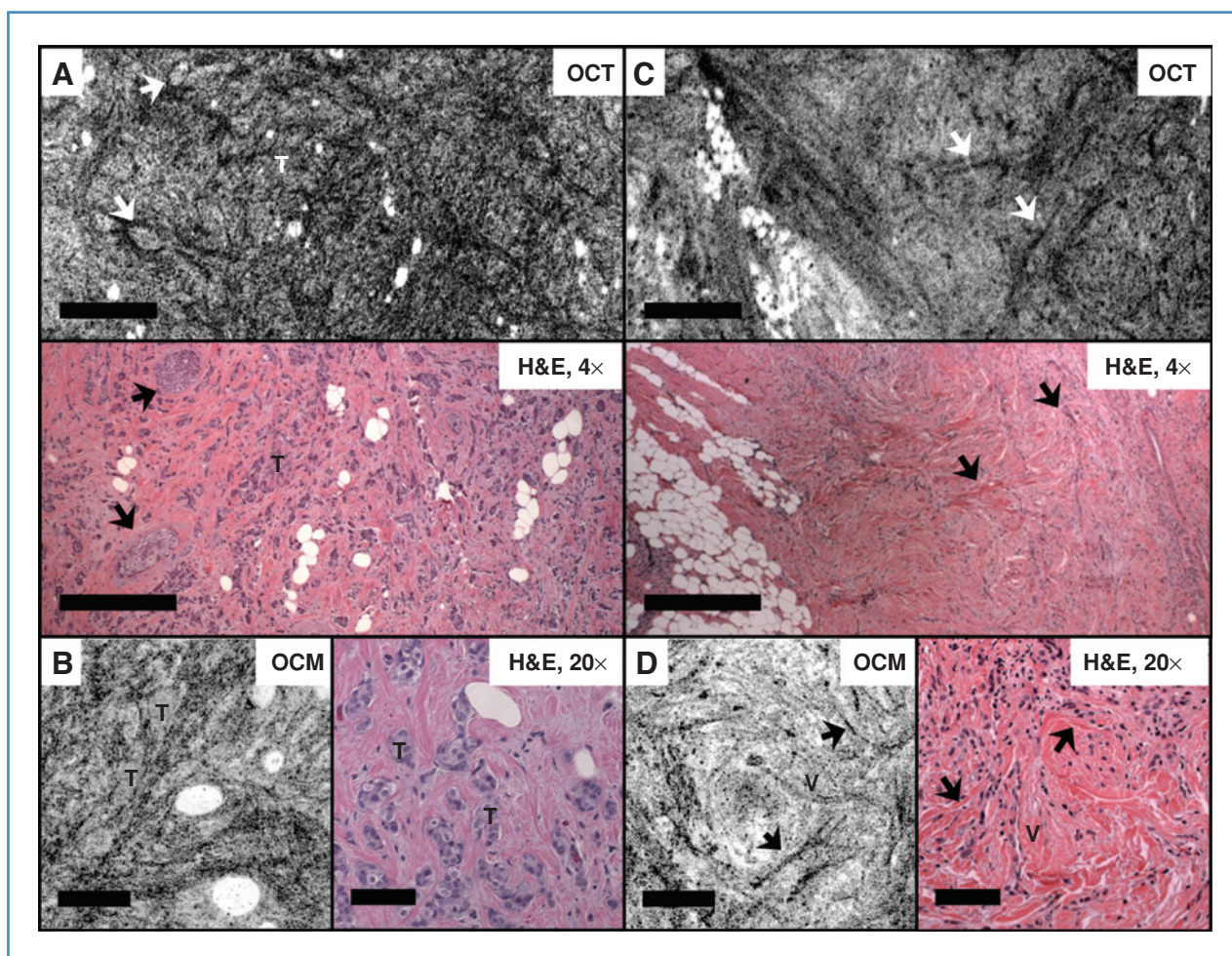


**Figure 5.** OCT, OCM images, and corresponding H&E histologic sections of invasive/*in situ* ductal carcinoma (A and B) and invasive lobular carcinoma (C and D). Arrows in A point to the DCIS involvement in invasive carcinoma. Arrows in C and D indicate stromal changes surrounding the characteristic cellular infiltration pattern of lobular carcinoma. T, tumor; V, microvessels. Scale bars, 500  $\mu$ m for OCT images and corresponding histology and 100  $\mu$ m for OCM images and corresponding histology. OCT images in A and C were reconstructed from  $\sim$ 70 and 180  $\mu$ m beneath the tissue surface, respectively. OCM images in B and D were within 50  $\mu$ m beneath the tissue surface.

*In situ* carcinoma can have a similar OCT/OCM appearance as benign breast lobules (as seen in Figs. 1 and 2); however, proliferating tumor cells in general may occlude the lumina of TDLUs and result in tightly packed cell clusters with no fine substructure observed with OCT or OCM. In the high-grade invasive ductal carcinoma case shown in Figure 6D, no normal tissue architecture is observed.

## Discussion

The OCT and OCM technologies presented in this study may be a useful complementary tool for real-time evaluation of breast lesions. Resolutions of OCT and OCM are 10–100 times finer than the state-of-the-art ultrasound technology. In our study, OCT and OCM successfully visualized characteristic features found in benign and malignant lesions of the human breast at multiple resolution scales without using

exogenous contrast agents or histologic processing. Distinctive OCT and OCM patterns were observed in adipose tissue, fibrous stroma, benign lobules and ducts, cysts, and *in situ* and invasive carcinoma. OCT and OCM provide complementary information about tissue microstructure. For example, architectural features associated with fibroadenoma, fat necrosis, and invasive carcinoma can be identified on low-magnification OCT images, whereas fine structures such as lumina within normal terminal ducts and lobules, microcysts, and clusters of tumor cells can be clearly observed on high-magnification OCM images. The images shown in the fat necrosis example (Fig. 3B) may not be easily differentiated from invasive carcinoma in the fat, such as the case in Figure 4B. However, calcification usually accompanies fat necrosis and is readily seen, which may be used as an imaging indicator to distinguish fat necrosis from invasive carcinoma in conjunction with other clinical information to assist differential diagnosis.



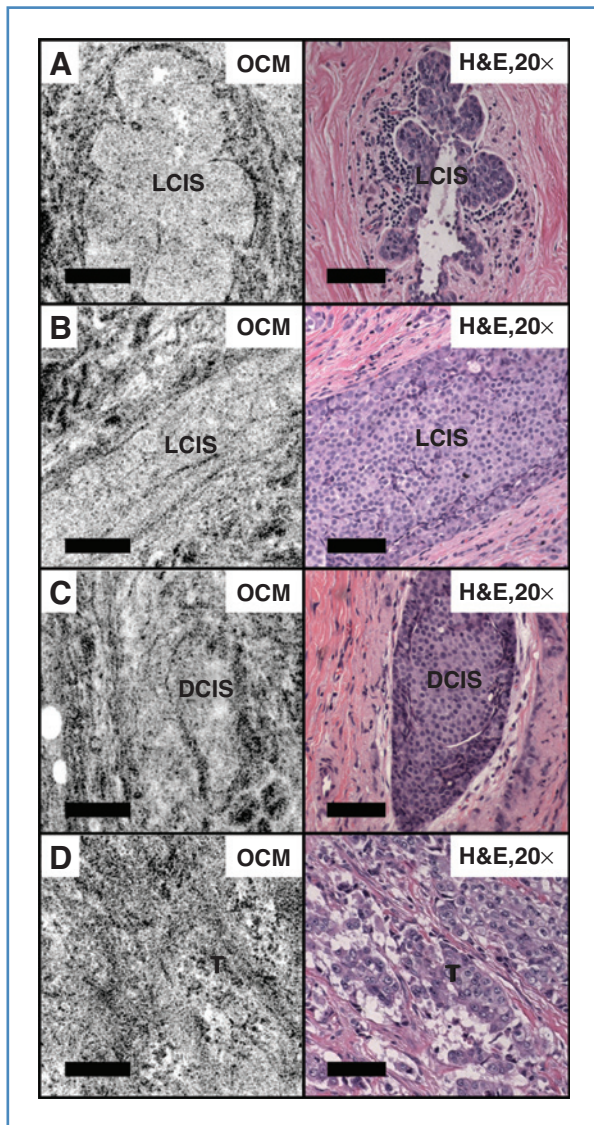


**Figure 6.** OCM images and corresponding H&E histologic section of LCIS (A and B), DCIS (C), and high-grade invasive ductal carcinoma (D). T, tumor; scale bars, 100  $\mu$ m. OCM images in A–D were within 50  $\mu$ m beneath the tissue surface. 3D-OCM reconstruction of LCIS in A and B can be found in the supplementary materials (Videos S3 and S4).

The capability of 3D imaging in OCT and OCM enables volumetric rendering of the tissue, which can be important for identifying characteristic features in various breast pathologies. 3D imaging provides complementary information to individual 2D OCT or OCM images and allows tracking features from different levels to identify 3D architecture and low-contrast structures that are difficult to appreciate from single images.

Consistent with previous findings (23), we have observed reduced scattering in cell-rich regions, such as normal lobules or tumors, compared with collagen-rich fibrous stroma. A previous study has suggested that occlusion of the lumina

together with the distortion of surrounding architecture could potentially be used to characterize ductal hyperplasia or carcinoma *in situ* (23). This is consistent with our current observations. We encountered cases in which distinguishing carcinoma *in situ* from normal breast lobules (Supplementary Fig. S1), which also have a high cellular density, was quite challenging. This is partly attributed to the limited optical contrast (tissue back-scattering contrast) available in standard OCT and OCM technologies. The development of polarization-sensitive OCT (PS-OCT; refs. 33–36) provides contrast based on tissue birefringence properties and can be a useful addition to OCT structural imaging. Moreover, novel OCT methods have been developed to utilize contrast agents, such as gold nanoparticles (37–40), which enable molecular-targeted imaging for early cancer detection.

Each year, about 1 million core biopsies are conducted for the diagnosis of breast cancer in the United States (10). During each core biopsy procedure, from 6 to 24 individual tissue cores are sampled from suspicious sites. There have been several efforts in developing miniature needle probes for OCT (41–43), which can potentially be integrated with a biopsy needle to guide tissue sampling. A preliminary assessment at the needle tip can therefore be made on the basis of imaging findings. A positive optical reading would indicate sampling from the lesion site. A negative reading would guide repositioning of the needle in order to minimize sampling from adjacent benign tissue. This approach would have the potential to improve the diagnostic accuracy of the procedure.

In breast tissue, *en face* OCT and OCM images with good contrast and resolution can be obtained from depths up to 300–400  $\mu$ m and 100–200  $\mu$ m beneath the tissue surface, respectively. This limitation is mainly due to multiple scattering in the tissues and optical aberrations as the imaging depth increases. Optical aberrations can be partially corrected by adaptive optics techniques, which may improve imaging depths (44, 45). In addition, imaging at a longer wavelength where the tissue scattering is reduced (e.g., 1,300 nm) would help to improve the imaging depth. However, for *in vivo* evaluation of microstructures several millimeters to centimeters deep inside the tissue, OCT and OCM technologies must be combined with needle-based imaging probes.

One limitation in the current imaging system is the slow imaging speed, which is not sufficient for *in vivo* applications. Advances in the development of Fourier-domain OCT techniques significantly improve (50–100 $\times$ ) the imaging speed and sensitivity (46–49). Recent results show that swept-source OCT can achieve 20M axial scans per second (50), enabling an entire 3D-OCT data set presented in this study to be obtained in a fraction of a second. These technological advances enable imaging speeds sufficient for future *in vivo* clinical applications.

This study is a preliminary investigation and the limited specimen number prevents us from carrying out an accurate statistical analysis of sensitivity and specificity for diagnosing breast cancers using OCT and/or OCM. Prospective studies with a larger sample cohort and blinded evaluation are

necessary to evaluate the detection accuracy associated with these new imaging technologies.

In summary, we show that OCT and OCM are capable of identifying characteristic imaging features in benign and malignant breast lesions, based on intrinsic optical contrast. OCT and OCM provide complementary information about tissue microstructure at multiple resolution scales, showing distinctive patterns for adipose tissue, fibrous stroma, normal breast lobules and ducts, cysts, and *in situ* and invasive carcinomas. The 3D imaging capability allows tracking features from different levels to identify 3D architecture and low-contrast structures that are difficult to appreciate from single images. These results lay the foundation for future *in vivo* optical evaluations of breast lesions, based on OCT and OCM technologies.

## References

1. American Cancer Society: Cancer Facts and Figures; 2010.
2. Silverstein MJ, Recht A, Lagios MD, et al. Image-detected breast cancer: state-of-the-art diagnosis and treatment. *J Am Coll Surg* 2009;209:504–20.
3. Parker SH, Burbank F, Jackman RJ, et al. Percutaneous large-core breast biopsy—a multi-institutional study. *Radiology* 1994;193:359–64.
4. Crowe JP, Rim A, Patrick RJ, et al. Does core needle breast biopsy accurately reflect breast pathology? *Surgery* 2003;134:523–6.
5. Dillon MF, Hill ADK, Quinn CM, O'Doherty A, McDermott EW, O'Higgins N. The accuracy of ultrasound, stereotactic, and clinical core biopsies in the diagnosis of breast cancer, with an analysis of false-negative cases. *Ann Surg* 2005;242:701–7.
6. Shah VI, Raju U, Chitale D, Deshpande V, Gregory N, Strand V. False-negative core needle biopsies of the breast—an analysis of clinical, radiologic, and pathologic findings in 27 consecutive cases of missed breast cancer. *Cancer* 2003;97:1824–31.
7. Agarwal T, Patel B, Rajan P, Cunningham DA, Darzi A, Hadjiminas DJ. Core biopsy versus FNAC for palpable breast cancers. Is image guidance necessary? *Eur J Cancer* 2003;39:52–6.
8. Jackman RJ, Nowels KW, Rodriguez-Soto J, Marzoni FA, Finkelstein SI, Shepard MJ. Stereotactic, automated, large-core needle biopsy of nonpalpable breast lesions: false-negative and histologic underestimation rates after long-term follow-up. *Radiology* 1999;210:799–805.
9. Parker SH, Jobe WE, Dennis MA, et al. US-guided automated large-core breast biopsy. *Radiology* 1993;187:507–11.
10. Liberman L, Feng TL, Dershaw DD, Morris EA, Abramson AF. US-guided core breast biopsy: use and cost-effectiveness. *Radiology* 1998;208:717–23.
11. Connolly JL, Boyages J, Nixon AJ, et al. Predictors of breast recurrence after conservative surgery and radiation therapy for invasive breast cancer. *Modern Pathol* 1998;11:134–9.
12. Gage I, Schnitt SJ, Nixon AJ, et al. Pathologic margin involvement and the risk of recurrence in patients treated with breast-conserving therapy. *Cancer* 1996;78:1921–8.
13. Park CC, Mitsumori M, Nixon A, et al. Outcome at 8 years after breast-conserving surgery and radiation therapy for invasive breast cancer: influence of margin status and systemic therapy on local recurrence. *J Clin Oncol* 2000;18:1668–75.
14. Fleming FJ, Hill ADK, McDermott EW, O'Doherty A, O'Higgins NJ, Quinn CM. Intraoperative margin assessment and re-excision rate in breast conserving surgery. *Eur J Surg Oncol* 2004;30:233–7.
15. Swanson GP, Rynearson K, Symmonds R. Significance of margins of excision on breast cancer recurrence. *Am J Clin Oncol-Cancer* 2002;25:438–41.
16. Krag D, Weaver D, Ashikaga T, et al. The sentinel node in breast cancer—a multicenter validation study. *New Engl J Med* 1998;339:941–6.
17. Mansel RE, Fallowfield L, Kissin M, et al. Randomized multicenter trial of sentinel node biopsy versus standard axillary treatment in operable breast cancer: the ALMANAC trial. *J Natl Cancer Inst* 2006;98:599–609.
18. Schrenk P, Rieger R, Shamiyeh A, Wayand W. Morbidity following sentinel lymph node biopsy versus axillary lymph node dissection for patients with breast carcinoma. *Cancer* 2000;88:608–14.
19. Olson TP, Harter J, Munoz A, Mahvi DM, Breslin TM. Frozen section analysis for intraoperative margin assessment during breast-conserving surgery results in low rates of re-excision and local recurrence. *Ann Surg Oncol* 2007;14:2953–60.
20. McLaughlin SA, Ochoa-Frongia LM, Patil SM, Cody HS, Sclafani LM. Influence of frozen-section analysis of sentinel lymph node and lumpectomy margin status on reoperation rates in patients undergoing breast-conservation therapy. *J Am Coll Surg* 2008;206:76–82.
21. Huang D, Swanson EA, Lin CP, et al. Optical coherence tomography. *Science* 1991;254:1178–81.
22. Boppart SA, Luo W, Marks DL, Singletary KW. Optical coherence tomography: feasibility for basic research and image-guided surgery of breast cancer. *Breast Cancer Res Treat* 2004;84:85–97.
23. Hsiung PL, Phatak DR, Chen Y, Aguirre AD, Fujimoto JG, Connolly JL. Benign and malignant lesion in the human breast depicted with ultrahigh resolution and dimensional optical coherence tomography. *Radiology* 2007;244:865–74.
24. McLaughlin RA, Scolaro L, Robbins P, Hamza S, Saunders C, Sampson DD. Imaging of human lymph nodes using optical coherence tomography: potential for staging cancer. *Cancer Res* 2010;70:2579–84.
25. Nguyen FT, Zysk AM, Chaney EJ, et al. Intraoperative evaluation of breast tumor margins with optical coherence tomography. *Cancer Res* 2009;69:8790–6.
26. Izatt JA, Hee MR, Owen GM, Swanson EA, Fujimoto JG. Optical coherence microscopy in scattering media. *Opt Lett* 1994;19:590–2.
27. Aguirre AD, Hsiung P, Ko TH, Hartl I, Fujimoto JG. High-resolution optical coherence microscopy for high-speed, *in vivo* cellular imaging. *Opt Lett* 2003;28:2064–6.
28. Huang SW, Aguirre AD, Huber RA, Adler DC, Fujimoto JG. Swept source optical coherence microscopy using a Fourier domain mode-locked laser. *Opt Express* 2007;15:6210–7.
29. Izatt JA, Kulkarni MD, Wang H-W, Kobayashi K, Sivak MV Jr. Optical coherence tomography and microscopy in gastrointestinal tissues. *IEEE J Sel Top Quant* 1996;2:1017–28.
30. Aguirre AD, Chen Y, Bryan B, et al. Cellular resolution *ex vivo* imaging of gastrointestinal tissues with optical coherence microscopy. *J Biomed Opt* 2010;15:016025;1–9.
31. Zhou C, Wang Y, Aguirre AD, et al. *Ex vivo* imaging of human thyroid pathology using integrated optical coherence tomography and optical coherence microscopy. *J Biomed Opt* 2010;15:016001;1–9.

## Disclosure of Potential Conflicts of Interest

J.G.F. receives royalties from intellectual property owned by MIT and licensed to Lightlab Imaging, Inc., and Carl Zeiss Meditec.

## Grant Support

This work was supported by the NIH grants R01-CA75289-13 (J.G.F. and J.L.C.), Air Force Office of Scientific Research contract FA9550-07-1-0014 (J.G.F.), Medical Free Electron Laser Program contract FA9550-07-1-0101 (J.G.F.), and the MIT/CIMIT Medical Engineering Fellowship and Taiwan Merit Scholarship from the National Science Council of Taiwan (T.H.T.).

The costs of publication of this article were defrayed in part by the payment of page charges. This article must therefore be hereby marked *advertisement* in accordance with 18 U.S.C. Section 1734 solely to indicate this fact.

Received 08/04/2010; revised 10/12/2010; accepted 10/26/2010; published OnlineFirst 11/05/2010.



32. Aguirre AD. *Advances in Optical Coherence Tomography and Microscopy for Endoscopic Applications and Functional Neuroimaging*. Cambridge, MA: Massachusetts Institute of Technology; 2008.
33. Hee MR, Huang D, Swanson EA, Fujimoto JG. Polarization-sensitive low-coherence reflectometer for birefringence characterization and ranging. *J Opt Soc Am B* 1992;9:903–8.
34. deBoer JF, Milner TE, vanGemert MJC, Nelson JS. Two-dimensional birefringence imaging in biological tissue by polarization-sensitive optical coherence tomography. *Opt Lett* 1997;22:934–6.
35. Everett MJ, Schoenenberger K, Colston BW, Da Silva LB. Birefringence characterization of biological tissue by use of optical coherence tomography. *Opt Lett* 1998;23:228–30.
36. Strasswimmer J, Pierce MC, Park BH, Neel V, de Boer JF. Polarization-sensitive optical coherence tomography of invasive basal cell carcinoma. *J Biom Opt* 2004;9:292–8.
37. Loo C, Lin A, Hirsch L, et al. Nanoshell-enabled photonics-based imaging and therapy of cancer. *Technol Cancer Res Treat* 2004;3:33–40.
38. Adler DC, Huang SW, Huber R, Fujimoto JG. Photothermal detection of gold nanoparticles using phase-sensitive optical coherence tomography. *Opt Express* 2008;16:4376–93.
39. Skala MC, Crow MJ, Wax A, Izatt JA. Photothermal optical coherence tomography of epidermal growth factor receptor in live cells using immunotargeted gold nanospheres. *Nano Lett* 2008;8:3461–7.
40. Zhou C, Tsai TH, Adler DC, et al. Photothermal optical coherence tomography in *ex vivo* human breast tissues using gold nanoshells. *Opt Lett* 2010;35:700–2.
41. Li X, Chudoba C, Ko T, Pitris C, Fujimoto JG. Imaging needle for optical coherence tomography. *Opt Lett* 2000;25:1520–2.
42. Zysk AM, Marks DL, Liu DY, Boppart SA. Needle-based reflection refractometry of scattering samples using coherence-gated detection. *Opt Express* 2007;15:4787–94.
43. Iftimia NV, Mujat M, Ustun T, Ferguson RD, Danthu V, Hammer DX. Spectral-domain low coherence interferometry/optical coherence tomography system for fine needle breast biopsy guidance. *Rev Sci Instrum* 2009;80:024302.
44. Rueckel M, Mack-Bucher JA, Denk W. Adaptive wavefront correction in two-photon microscopy using coherence-gated wavefront sensing. *Proc Natl Acad Sci USA* 2006;103:17137–42.
45. Debarre D, Botcherby EJ, Watanabe T, Srinivas S, Booth MJ, Wilson T. Image-based adaptive optics for two-photon microscopy. *Opt Lett* 2009;34:2495–7.
46. Fercher AF, Hitzinger CK, Kamp G, Elzaiat SY. Measurement of intraocular distances by backscattering spectral interferometry. *Opt Commun* 1995;117:43–8.
47. Choma MA, Sarunic MV, Yang CH, Izatt JA. Sensitivity advantage of swept source and Fourier domain optical coherence tomography. *Opt Express* 2003;11:2183–9.
48. de Boer JF, Cense B, Park BH, Pierce MC, Tearney GJ, Bouma BE. Improved signal-to-noise ratio in spectral-domain compared with time-domain optical coherence tomography. *Opt Lett* 2003;28:2067–9.
49. Leitgeb R, Hitzinger CK, Fercher AF. Performance of Fourier domain vs. time domain optical coherence tomography. *Opt Express* 2003;11:889–94.
50. Wieser W, Biedermann B, Klein T, Eigenwillig C, Huber R. Multi-Megahertz OCT: high quality 3D imaging at 20 million A-scans and 4.5 GVoxels per second. *Opt Express* 2010;18:14685–704.